



Function-oriented defect assessment in hybrid sheet molding compound tensile specimen using surrogate models

Lucas Bretz^{1,2} · Dominik Koch¹ · Krzysztof Debowski¹ · Katja Höger¹ · Gisela Lanza^{1,2}

Received: 7 September 2022 / Accepted: 21 November 2022
© The Author(s) 2022

Abstract

Glass fiber (GF) Sheet Molding Compound (SMC) composites are popular lightweight materials due to their good processability. Hybrid SMCs expand the field of operation, combining the high stiffness of unidirectional carbon fibers (CF) with the economic efficiency of GF. Combinations of manufacturing deviations (delamination, varying GF content, CF misorientation) occur during the production of hybrid SMCs and impede the mechanical performance of the part. A function-oriented quality assurance instead of strict tolerances is proposed. Finite element (FE) simulations are computationally too expensive for an assessment within the cycle time. Hence, surrogate models are trained on multiple parameterized FE simulations. The surrogate models shall allow for an individual functional assessment in real-time based on integrated measurement inputs. This work focuses on the generation of parametrized FE simulations for measurement inputs and surrogate modeling. Simulations and surrogate models show acceptable deviations from tensile tests for multiple combinations of manufacturing deviations. The measurement uncertainty of the stiffness prediction is assessed for both the FE simulation and the surrogate models in accordance with the Guide to the Expression of Uncertainty in Measurement (GUM).

Keywords Fiber reinforced polymer · Non-destructive testing · In-line measurement · Quality assurance · Surrogate model · Finite element simulation

1 Introduction and motivation

Lightweight construction plays an essential role to reduce overall CO₂ emissions [1]. Fiber reinforced polymers (FRP) combine high mechanical stiffness and strength with lower weight compared to metals. Multi-material designs are developed to economically tailor the mechanical properties to the specific requirements of the part. Sheet Molding Compound (SMC) is the FRP of highest economic importance considering production volume in Europe [2]. The usage of continuous (Co) and discontinuous (DiCo) fibers in a fiber reinforced polymer (CoDiCoFRP) introduces a new hybrid material class. Continuous fibers offer better mechanical properties while discontinuous fibers improve processability [3].

SMC is typically produced on a conveyor belt. Chopped glass fibers (GF) are sandwiched between an upper and lower layer of thermoset resin. Thus, a mostly planar isotropic fiber orientation distribution (FOD) can be assumed for the semi-finished DiCo-SMC. Calendaring ensures the resin impregnation of all fibers. The material is matured to reach an increased viscosity stage, called B-stage or prepreg. The same procedure holds to produce unidirectional carbon fiber SMC (Co-SMC), except it is not cut and the unidirectional fiber orientation is maintained between the resin layers. In the co-molding process, a layered structure, consisting of multiple DiCo-SMC layers and patches of Co-SMC, is placed in the mold of a hot press and cured [3].

Various manufacturing deviations affect the mechanical properties of the CoDiCoFRP [4]. Manufacturing deviations are mostly considered as defects and lead to a rejection of the part, but could alternatively be considered as individual characteristics of the part [5]. However, the significance of manufacturing deviations varies with the local performance requirements of the part. Manufacturing deviations could be allowed if the function of the part is not impeded. Thus, manufacturing costs of FRPs could drastically be reduced.

✉ Lucas Bretz
lucas.bretz@kit.edu

¹ Karlsruhe Institute of Technology (KIT), wbk Institute of Production Science, Karlsruhe, Germany

² Global Advanced Manufacturing Institute (GAMI, KIT China Branch), Suzhou, China

An individual part characterization and functional assessment are indispensable to allow manufacturing deviations. Multiple in-line measurement techniques are required to quantify potential manufacturing deviations within the cycle time. The measurement results need to be fed into a functional evaluation routine, such as a finite element (FE) simulation. However, FE simulations require high computational effort. Various surrogate models proved to be accurate enough for representing FE simulations, while significantly reducing computational effort (cf. Sect. 2.3). An individual component assessment could be enabled with the help of in-line measurements and surrogate models.

2 State of the art

2.1 Effects of defects in fiber reinforced polymers

Voids [3, 5], delaminations [3, 6], fiber misorientations [3, 4, 6] and deviations of local fiber content [7] are common manufacturing deviations of FRPs. Voids and a reduced fiber content lead to reduced strength [3, 8] and stiffness [5, 8]. Schäferling et al. experimentally investigated the influence of various manufacturing deviations in CoDiCoFRP tensile tests on the Young's modulus and the tensile strength [6]. Hybrid coupon specimens with delaminations showed only a slightly decreased tensile strength. Fiber misorientations reduced the stiffness and the tensile strength. No simulative approach and no interaction of defects was considered in this investigation. Fengler et al. conducted a robustness study for CF patch placement while considering the simulated stiffness of the part under patch misplacement [4]. Franz et al. investigated the influence of fiber misorientations in a laminate layup to support the design engineer in tolerancing FRP-parts [9, 10]. Kehrer et al. developed a Mori–Tanaka homogenization scheme based on orientation average for DiCo-SMC, taking into account the FOD and the fiber content [11].

2.2 Function-oriented measurement

Weckenmann and Hartmann introduced the term “function-oriented measurement” in the context of geometric product specification [12, 13]. A mathematical-physical model, fed with measurement results, was proposed. This model could serve as a “virtual functional gauge” and allowed the assessment of multiple measurement results by quantitatively predicting the functional ability of the product. Wagner et al. introduced adaptive quality control strategies for high-pressure injectors based on FE simulations and in-line measurement results [14]. Gauder et al. proposed a function-oriented evaluation for the acoustic emissions of micro gears based on in-line topographical measurements and FE

simulations [15]. Talreja suggested an acceptance of FRPs based on their mechanical performance instead of binary acceptance criteria. Thus, the material state (combination of defects) needs to be characterized and evaluated by means of simulation [5].

2.3 Surrogate models of FE simulations

Sinsberg defines surrogate models as a “function that behaves similarly to the original function or simulation in terms of its input–output relation, but is much faster to evaluate” [16]. Artificial Neural Networks (ANN) [17], Deep Neural Networks [18], long-short term memory (LSTM) models [19], Proper Orthogonal Decomposition [20] and Kriging models [4, 10, 21] proved to be successful for surrogate modeling FE simulations. A detailed performance study of different surrogate model techniques and sampling methods using a CFRP plate as an example exists [22]. A review on surrogate modeling techniques and sources of uncertainty is given in Ref. [23]. Surrogate models have so far been used primarily in the design phase in the context of FRP product development [4, 10]. To the author's knowledge, an individual FRP component evaluation based on in-line measurement results does not exist. The authors chose to work with ANNs and Kriging models in this work because of references for function-oriented measurements [17] and the material formulation under investigation [4]. A detailed comparison regarding suitability of different surrogate modeling techniques with respect to measurement integration is not performed within this work.

2.4 Measurement uncertainty

A standardized procedure for the determination of measurement uncertainties has been defined in the international Guide to the Expression of Uncertainty in Measurement (GUM) [24]. The expanded uncertainty U (cf. Eq. (1)) describes the level of confidence that the measurement results lie within a large fraction of the interval about the measurement result:

$$U = k \cdot u_c; \quad (1)$$

with the coverage factor k and the combined uncertainty u_c .

Supplement 1 of the GUM describes a procedure to calculate the measurement uncertainty with the means of Monte-Carlo simulations instead of a linearization and a Taylor approximation [25]. According to Lord and Wright, the uncertainties of FE models can be categorized into four groups [26]:

- (1) Model's description of reality is not exact
- (2) Model discretization is an inexact approximation

- (3) Uncertainty of model input values
- (4) Algebraic solution is not exact

The uncertainty of surrogate models composes of:

- (1) Uncertainties of model input values [27, 28]
- (2) Model uncertainties based on existing training data [27, 28]
- (3) Systematic model deviation [28, 29]

In this contribution, the Young's modulus as an output of the FE simulations and the surrogate models is considered as a measurement itself. Only the model discretization and the uncertainty contributions of the input values are taken into account for the determination of the uncertainty of the FE model, because modeling and solution errors are typically insignificant [26]. All three sources of uncertainty are considered for the surrogate model.

Overall, widening the tolerances could drastically reduce the costs for manufacturing FRPs. Considering the presented defects as an individual state of the part while evaluating their influence on mechanical performance could serve as a virtual functional gauge. So far, the combinations of multiple defects in hybrid FRPs were neither investigated in experiments nor in simulations.

3 Approach

3.1 Overview

Figure 1 illustrates the general idea of an individual function-oriented part assessment. Functional requirements determine the part design and its dimensioning. However, production processes are not ideal and manufacturing deviations, as described in Sect. 2, occur. In-line measurements enable the determination of the individual part condition. Integrating those individual measurement results into FE simulations, originating from the product design process,

could allow for an individual assessment based on the realized function. Because of the computational effort, FE simulations do not meet the requirements of an assessment within the cycle time. Thus, multiple parametrized FE simulations shall be used to train a surrogate model which allows a functional assessment in real-time based on measurement inputs. This work focuses on the generation of parametrized FE simulations for measurement inputs and surrogate modeling. The following subsections describe the detailed approaches for the specimen design, the development of the FE model including a measurement uncertainty evaluation and the training of two different surrogate model approaches [28].

3.2 Tensile test specimens

Multiple plates (458 mm × 458 mm) with varying glass fiber mass fraction (FMF) of DiCo-SMC were manufactured. Optionally, a Co-SMC layer (CF) was added in the stacking process. The resin of the DiCo-SMC and the Co-SMC layer is based on an unsaturated polyester polyurethane hybrid (UPPH) resin. Glass fiber length was 25.4 mm with a fiber diameter of 13.5 μm. Three different B-stage materials with different glass fiber mass contents were considered (41, 45 and 50 wt%). A single layer of semi-finished material (prepreg) was approximately 1 mm thick. Two layers of DiCo-SMC prepreg were stacked. Artificial delaminations, consisting of a 130 μm thick Teflon (PTFE) foil, were optionally integrated between the individual Co-SMC layers. Artificial voids should be integrated by incorporating 100 mg of the propellant ammonium bicarbonate between the two layers of DiCo-SMC. However, the propellant led to surface damages and voids which could not be reproducibly integrated into the specimens. Thus, the integration of voids was discarded. A layer of Co-SMC was only placed on top of the DiCo-SMC when hybrid SMC plates were manufactured. The mold cavity was fully covered to minimize material flow. Thus, the planar isotropic fiber orientation distribution (FOD) from the prepreg production process was maintained. The mold was heated to 145 °C and closed

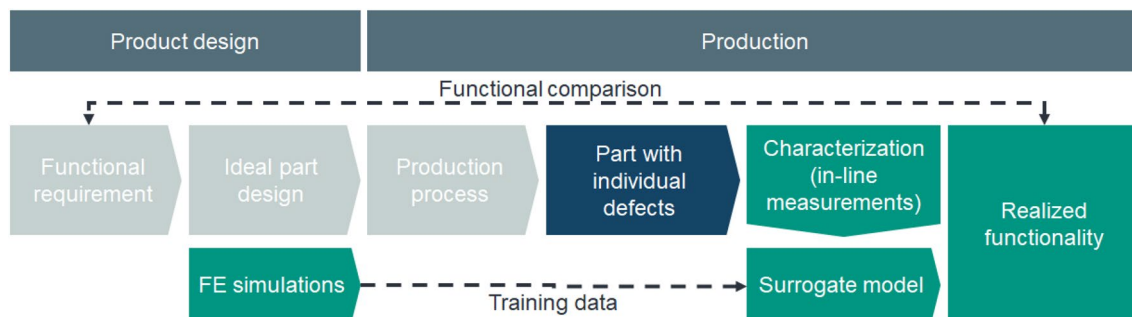


Fig. 1 Function-oriented approach for the individual assessment of FRP parts

with a maximum hydraulic press force of 500 kN. After co-molding, coupon specimens with a length of 200 mm, a width of 15 mm and a thickness of approximately 2 mm were waterjet cut from all plates. 10° and 20° fiber misorientations of the Co-SMC layer were realized through the waterjet cut. Thus, different tensile specimens with varying manufacturing deviations were realized (cf. Table 1). Each configuration consisted of at least 15 samples. An exemplary specimen is shown in Fig. 2c. The average thickness of every

configuration was calculated based on three measurements per sample [28].

3.3 Experimental procedure

The tensile tests were carried out on a ZwickRoell Zmart. Pro universal testing machine with a load cell capacity of 200 kN. The clamping length was 50 mm on each side of the specimen. Specimens were preloaded up to 100 N. Afterwards, they were loaded with a nominal loading rate of 1 mm/min until failure. Young’s modulus was determined using a least squares method in a strain range between 0.05 and 0.25% [30]. Tensile strength was determined by an abrupt load drop of 8 MPa. Only specimens that failed in sufficient distance from the clamping area were considered. At least five specimens were taken for the evaluation of tensile strength for each specimen configuration [28].

Table 1 Different configurations of tensile specimen with manufacturing deviations including specimen thickness [28]

Configuration no.	Configuration name	Prepreg fiber mass content (wt%)	Orientation of co-SMC layer (°)	Delamination size (mm) × mm)	Average thickness [standard deviation] (mm)
1	41	41	–	–	1.76 [0.03]
2	41.M10	41	–	10×15	1.90 [0.03]
3	41.M20	41	–	20×15	1.89 [0.03]
4	41.0	41	0	–	2.26 [0.02]
5	41.0.M10	41	0	10×15	2.09 [0.02]
6	41.20	41	20	–	2.22 [0.02]
7	41.20.M20	41	20	20×15	2.14 [0.04]
8	41.10	41	10	–	2.19 [0.04]
9	41.10	45	–	10×15	2.32 [0.02]
10	45.M10	45	20	–	2.36 [0.02]
11	45.20	50	–	–	2.49 [0.02]
12	50	50	–	20×15	2.49 [0.03]
13	50.M20	50	0	–	2.55 [0.06]
14	50.0	50	0	20×15	2.61 [0.04]
15	50.0.M20	50	20	–	2.73 [0.05]
16	50.20.M20	50	20	20×15	2.14 [0.06]

3.4 Finite element simulation

The commercial software Abaqus FEA from Dassault Systèmes was used to parametrically model the hybrid specimen including potential manufacturing deviations. The DiCo- and Co-SMC were represented by two distinguished, perfectly bonded, parts. Solid elements for the DiCo-SMC and continuum shell elements for the Co-SMC layer were used. Isotropic material behavior was assumed both for the glass fiber and the resin. Void content was analytically integrated into the resin [31]. A Mori–Tanaka homogenization based on orientation average (planar isotropic FOD) and fiber content was performed for calculating the linear elastic material properties of the DiCo-SMC [11]. Five different regions for assigning local variations of the glass fiber content were defined. The Co-SMC layer was modeled

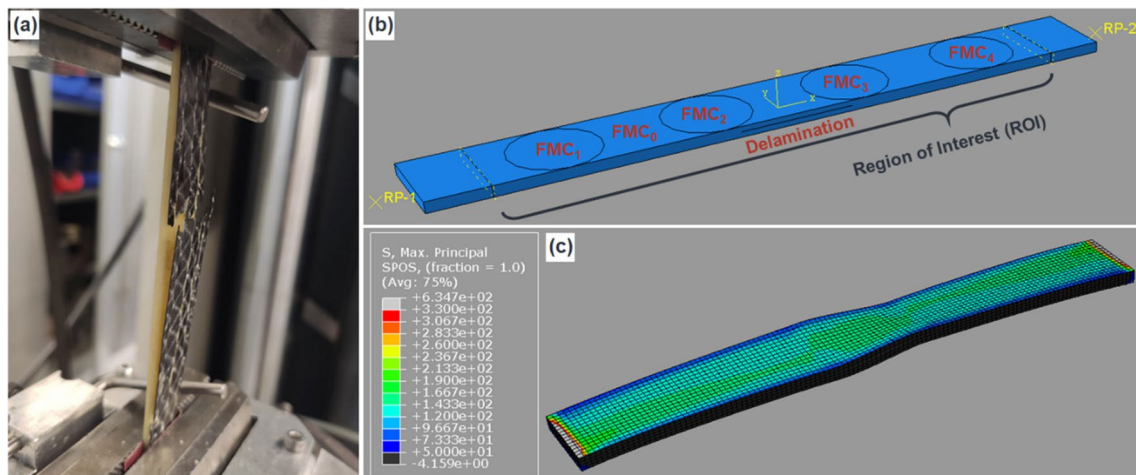


Fig. 2 a Specimen in tensile testing machine; b Local regions for varying GF regions and integrated delamination in DiCo-SMC; c Stress distribution and enhanced twisting of the specimen in the presence of CF patch misorientation

using five independent material parameters, describing a transverse isotropy. Engineering constants were used in Abaqus. The Extended Finite Element Method (XFEM) was used to model delaminations in the DiCo-SMC. The initial delamination was modeled as a shell and placed within the solid elements of DiCo-SMC. The five regions of varying GF content and an integrated delamination are visualized in Fig. 2b. A maximum principal stress criterion was chosen. The maximum principal stress was determined with a least squares method for different fiber contents. Critical energy release rates were used in a Benzeggagh-Kenane (BK) law for a single scalar fracture criterion. The critical release energy was experimentally determined in a double cantilever beam (DCB) test [28]. Failure in the Co-SMC layer was modeled using a publicly available Abaqus user subroutine of the Puck criterion [32].

The tensile specimen was FE modeled with an overall length of 120 mm and a width of 15 mm. 10 mm were reserved as a clamping area at each side. Thus, the lengths of the region of interest are both 100 mm in the simulations and experiments. The DiCo-SMC model thickness was individually adjusted according to the averaged measured specimen thickness. The patch thickness was kept constant at its nominal thickness of 0.3 mm. The end edge of each clamping area was tied to a reference point (cf. Fig. 2b). One reference point was fixed, whereas the second reference point was subjected to a longitudinal force of 1500 N. Element side length was 0.77 mm (7500 elements in the ROI). A discretization study showed no significant further increase of strain energy after 3350 elements in the ROI [28]. The used material parameters are given in Table 8.

3.5 Measurement uncertainty of the FE model

The function-oriented evaluation of measurement results directly depends on the trustworthiness of the FE model. Thus, the measurement uncertainty of the Young's modulus according to the FE simulation shall be evaluated according to Eq. (2)

$$u_{c,Sim} = \sqrt{u_{Sim,I}^2 + u_{Sim,D}^2 + b_{Sim}^2}. \quad (2)$$

An iterative approach for the calculation of the uncertainty based on the input parameters $u_{Sim,I}^2$ was chosen, described in the next paragraph. $u_{Sim,D}$ represents the systematic deviation between the used discretization in the simulation study and a finer reference simulation according to the available computation power. The systematic model deviation (bias) b_{Sim} is given by the root mean squared error (RMSE), cf. Eq. (3) [29]. The mean experimental results \bar{y} was used to calculate a relative metric, in accordance with the coefficient of variation, cf. Eq. (4).

$$b_{Sim} = \sqrt{\frac{\sum_{t=1}^T (y - \hat{y}_{Sim})^2}{T}}. \quad (3)$$

$$CV_{RMSE} = \frac{RMSE}{\bar{y}}. \quad (4)$$

Initially, a screening experiment was conducted, in which all considered input parameters of the hybrid SMC (cf. Table 9) were increased by one standard uncertainty. One factor at a time was varied. Input factors leading to a minor deviation of 0.5% or less from the simulated reference Young's modulus were discarded. Afterwards, the remaining parameters were subjected to a Latin Hypercube sampling (LHS) for generating varying realizations of the same specimen configuration according to the probability distribution of the different input parameters. The function $lhs()$ within the Python package *pyDOE* was used for generating the LHS. FE simulations were conducted for every specimen composition, leading to different stiffness outputs from the multiple FE simulations (110 to 140 simulations per specimen composition) [28]. The mean and the standard variation were calculated for every configuration based on the distributed values (cf. Sect. 4.2).

3.6 Kriging surrogate model

The randomly occurring manufacturing deviations represent individual part characteristics collected in the feature vector ω (set of manufacturing deviations), which are to be quantified using in-line measurements in later stages. Running individual, computational expensive FE simulations is not feasible while adhering to the cycle time. Thus, the surrogate model should enable a quick evaluation of measurement results and replace computational expensive simulations. A Kriging model was chosen in this contribution as one approach, because it allows the evaluation of the local error estimate produced by the model. Thus, the most promising training data in terms of reducing the model uncertainty shall be generated in subsequent FE simulations, further described in Sect. 3.6.1. The Python package *SMT: Surrogate Modeling Toolbox* was used in this contribution [33].

3.6.1 Generation of training data

Training data within the whole experimental space was needed for the generation of the surrogate model. The optional presence of patches and delaminations were considered as binary states of the specimen. Thus, four independent experimental designs were chosen for the four essential specimen compositions (DiCo-SMC, DiCo-SMC with delamination, hybrid SMC, hybrid SMC with delamination).

LHS was chosen to effectively cover the experimental space. The input parameters dependent on the specimen composition and their value domain are given in Table 2 [28].

The output values y were independently generated for the four essential specimen compositions (cf. Eq. (5)), based on the FE simulations. An individual Kriging model was trained for every row. Equation (5) displays row-wise the output values for the four essential specimen compositions, with the Young’s modulus \hat{E} , the Puck damage criteria $\hat{f}_{E,0}$, $\hat{f}_{E,1}$ and \hat{f}_E [34] in the Co-SMC, and the stress exposure $\hat{f}_{E,0}$ to $\hat{f}_{E,4}$ in the 5 different regions of the DiCo-SMC [28].

$$\begin{bmatrix} \hat{E} & - & - & - & \hat{f}_{E,0} & \hat{f}_{E,1} & \hat{f}_{E,2} & \hat{f}_{E,3} & \hat{f}_{E,4} \\ \hat{E} & - & - & - & \hat{f}_{E,0} & \hat{f}_{E,1} & \hat{f}_{E,2} & \hat{f}_{E,3} & \hat{f}_{E,4} \\ \hat{E} & \hat{f}_{E,0} & \hat{f}_{E,1} & \hat{f}_E & \hat{f}_{E,0} & \hat{f}_{E,1} & \hat{f}_{E,2} & \hat{f}_{E,3} & \hat{f}_{E,4} \\ \hat{E} & \hat{f}_{E,0} & \hat{f}_{E,1} & \hat{f}_E & \hat{f}_{E,0} & \hat{f}_{E,1} & \hat{f}_{E,2} & \hat{f}_{E,3} & \hat{f}_{E,4} \end{bmatrix} = \begin{bmatrix} y_{SMC} \\ y_{SMC+Delamination} \\ y_{HSMC} \\ y_{HSMC+Delamination} \end{bmatrix} \tag{5}$$

Training the Kriging model by an initially fixed number of generated values using LHS has the advantage of an even distribution of training data in the experimental space. Nevertheless, regions with a high model uncertainty occur. Thus, an iterative training approach was chosen to make use of the inherent uncertainty information of the Kriging model. Multiple rounds of consecutive training data, each round consisting of 80 additional data points (20 per specimen composition), were generated based on a search for the regions with the highest variances. The regions for the newly generated FE data were determined by regions with highest variances. However, a full factorial design for evaluating and assessing the current Kriging model would lead to an excessive runtime. Thus, a grid search based on a LHS with 5000 configurations was chosen for evaluating the variances of the current Kriging model. The regularized squared variances

of all output values of an essential specimen composition i are summed up according to Eq. (6) to find twenty configurations for each surrogate model composition (cf. Eq. (5)) that offer the largest improvement potential. This procedure was repeated until no further significant improvements were observed [28].

$$S_i^2 = S_{E,i}^2 + \sum_{k=4}^6 S_{Uk,i}^2 + \sum_{k=0}^4 S_{Mk,i}^2 \tag{6}$$

Additionally, a direct approach with evenly distributed training data within the experimental space was taken for reference. Its size was chosen to be the size after convergence (810 specimen configurations) [28].

3.6.2 Generation of test data

Three different test sets were generated. A first test set P_1 was generated using LHS to evaluate the performance over the whole value domains (cf. Table 2). LHS ensured an even distribution in the parameter space. Its size was 20% of the training set for each specimen composition. FE simulations were run for each test data point and compared to the Kriging prediction for each entry in the matrix of Eq. (2). A second test set (virtual experiments, P_2) was generated using FE simulations based on the experimental configurations (cf. Table 1) to evaluate the performance of the Kriging model. The maximum $max[U_4, U_5, U_6, \hat{f}_{E,0}, \hat{f}_{E,1}, \hat{f}_{E,2}, \hat{f}_{E,3}, \hat{f}_{E,4}]$ was used for each configuration to calculate the tensile strength using the reciprocal stress exposure (stretch factor). Thirdly, the results were compared to the physical experiments P_3 ,

Table 2 Considered input parameters and their value domain for the four essential specimen compositions [28]

	DiCo-SMC	DiCo-SMC and delamination	Hybrid SMC	Hybrid SMC and delamination	Value domain
FMC ₀	X	X	X	X	[30, 55] wt%
FMC ₁	X	X	X	X	[30, 55] wt%
FMC ₂	X	X	X	X	[30, 55] wt%
FMC ₃	X	X	X	X	[30, 55] wt%
FMC ₄	X	X	X	X	[30, 55] wt%
Thickness of SMC	X	X	X	X	[1.75, 2.5] mm
Porosity ₀	X	X	X	X	[0, 5] vol%
Porosity ₁	X	X	X	X	[0, 5] vol%
Porosity ₂	X	X	X	X	[0, 5] vol%
Porosity ₃	X	X	X	X	[0, 5] vol%
Porosity ₄	X	X	X	X	[0, 5] vol%
CF Angular deviation			X	X	[0, 20] °
Delamination length		X		X	[5, 50] mm
Position of delamination		X		X	[- 25, 25] mm

allowing a direct assessment of the suitability for a real-world application [28].

3.7 Artificial neural network

An artificial neural network (ANN) was chosen as a second approach in this contribution, because it allows a vector-valued input and deals with binary conditions, such as the presence of a patch or a delamination. Thus, the complexity of the surrogate model itself is drastically reduced from the user’s perspective. A fully connected multilayer perceptron was built using tensorflow’s keras. Each of the 21 input neurons represented one parameter of the input file for the FE simulation. Three hidden layers, each built of 18 neurons, were chosen based on best model performance among different network configurations in a trial and error process. The output layer consisted of 9 neurons, like the rows of the matrix in Eq. (2) [28].

3.7.1 Generation of training and test data

The training dataset of the Kriging model was also used for the training process of the ANN. The dataset was randomly split into 80% training data and 20% development data as a measure for the loss function. The mean squared error (MSE) was used as a metric for the loss function. The ANN was trained in 1500 epochs with a batch size of 50. Early stopping was initiated when no significant improvements were observed in 20 consecutive epochs to prevent overfitting. Adam was utilized as optimization algorithm. The same three test sets were used to evaluate the performance of the ANN [28].

3.8 Measurement uncertainty of the surrogate models

Overall, the combined uncertainty of a surrogate model $u_{c,SM}$ is calculated as given in Eq. (7). Correlations of individual terms are neglected.

$$u_{c,SM} = \sqrt{u_{SM,I}^2 + u_{SM,T}^2 + b^2} \tag{7}$$

3.8.1 Standard uncertainty due to input quantities

The same quantities as in the measurement uncertainty analysis of the FE simulation were considered again (cf. Table 9). The evaluation of the surrogate models was significantly faster compared to the FE simulation. Hence, a screening was omitted. $q = \{1, \dots, Q\}$ different combinations

of realized input variables for each configuration from the test data set P were drawn according to their probability density function (PDF) and propagated through the surrogate models. The variable Q was 10 times the number of input variables and depended on the specimen composition (cf. Table 2). Hence, a normal distribution based on uncertain input quantities was obtained for each of the C configurations in the test data set. The mean value was calculated and led to $u_{SM,I}$ [28].

3.8.2 Standard uncertainty due to model training

The influence of variability in training data on an ANN can be determined based on repeated realizations of slightly different ANNs, an ANN committee with random changes in training data [27]. The training data set T_L , generated by LHS, was enlarged by 10% of its original size using Monte Carlo method (MCM) for generating the substitutional set T_M . Then, $R = 100$ combinations of different training data sets were drawn from the overall available set. The size for each training set remained the same as in the original one T_L . The test sets P were propagated through the ANN committee, leading to normally distributed function predictions for the C different configurations. Hence, the ANN training uncertainty was determined according to Eq. (8). The overall procedure is visualized in Fig. 6.

$$u_{SM,T,ANN} = \frac{1}{C} \sum_{i=1}^C u_{SM,T,i} \tag{8}$$

For the Kriging model, the respective uncertainty was determined based on the local model variances at $G = 5000$ randomly generated test points (cf. Sect. 3.6.1) and subsequently averaged [28]:

$$u_{SM,T,Kriging} = \frac{1}{G} \sum_{i=1}^G u_{SM,T,i} \tag{9}$$

3.8.3 Surrogate model bias

The difference between the scalar function prediction (Young’s modulus) of the surrogate model \hat{y}_{SM} and the test set \hat{y}_{test} was assessed by the RMSE as follows [28]:

$$b_{P_i} = RMSE(P_i) = \sqrt{\frac{\sum_{k=1}^{K_i} (\hat{y}_{test,i,k} - \hat{y}_{SM,i,k})^2}{K_i}}, \tag{10}$$

for $\begin{cases} i = \{1;2;3\} \\ \hat{y}_{test,i} = \{\hat{y}_{Sim,P_1}; \hat{y}_{Sim,P_2}; \hat{y}_{P_3}\} \end{cases}$

4 Results

4.1 Experimental results and FE simulations

Experimental results and simulations for the Young’s modulus are given in Fig. 3. FE simulations show an overall $RMSE$ of 1.34 GPa (coefficient of variation: $CV_{RMSE} = 7.8\%$). The simulation systematically overestimated the Young’s modulus for configurations with 50 wt% FMF. This behavior indicates an insufficient impregnation of fibers for these high FMFs when compared to configurations with 41 and 45 wt%. These configurations showed a significantly lower $RMSE$ of 0.65 GPa ($CV_{RMSE} = 3.8\%$) compared to the configurations 11 to 16 ($RMSE = 1.88$ GPa, $CV_{RMSE} = 10.8\%$). Overall, it can be concluded that the FE model predicted the stiffness well for the first 10 configurations [28].

The experimental results for tensile strength are compared with the simulated results in Fig. 7. Acceptable results were only obtained for configurations of pure DiCo-SMC or for high Co-SMC misorientations of 20° (specimen no. 1, 7, 8). The nominal longitudinal tensile strength of the Co-SMC caused an overestimation of the hybrid material composition (cf. configuration 41.0). Here, a single layer Co-SMC (0.3 mm thickness) was used in contrast to the experimental investigation of the material properties of a Co-SMC specimen (1 mm thickness, [35]). Comparing configurations 41.20 and 41.20.M20 (specimen no. 7 and 8), the failure was well described. The delamination caused

a bulging of the specimen (cf. Fig. 2c), locally increasing the stress distribution and leading to an earlier failure. The longitudinal tensile strength had a minor influence on failure due to the misorientation of the Co-SMC patch. The existing deviations in tensile strength between experiment and simulation for pure DiCo-SMC (41) and DiCo-SMC plus delamination (41.M10) indicate that further micromechanical effects exist, which are not correctly represented by a solely geometric integration of delamination into a homogenized DiCo-SMC material [28]. The bias is summarized for both Young’s modulus and tensile strength in Table 3.

4.2 Measurement uncertainty of the FE model

Five representative specimen configurations were considered for the measurement uncertainty analysis. Specimen configurations with different nominal glass FMF and different combinations of patch orientation and delamination were chosen. The screening analysis (one factor at a time) showed that nine input parameters could be neglected based on their relative significance below 0.5%. Hence, six to eight parameters remained, dependent on the configuration (cf. Table 4).

The influence of voids was not relevant if the CF patch was mostly loaded in fiber direction. Accordingly, standard uncertainties of measured CF patch orientation were not relevant when loaded in fiber direction. The generated realizations of simulations based on varying input parameters led to normal distributed results for the Young’s modulus. The

Fig. 3 Experimental and simulated Young’s modulus for CoDiCo-SMC tensile specimen; error bars indicate one standard deviation; configuration no. in parenthesis; according to Ref. [28]

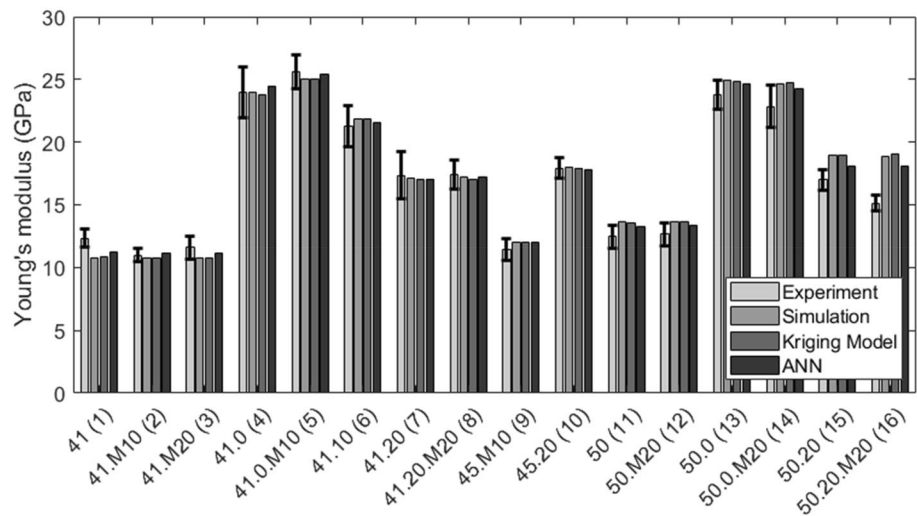


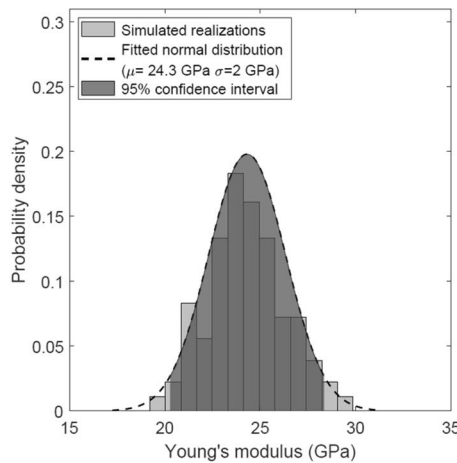
Table 3 Systematic deviations (bias) of the FE simulation for CoDiCo-SMC tensile specimen; CV_{RMSE} given in percentage [26]

Included configurations for calculation of	No. 1 to 16		No. 1 to 10		No. 11 to 16	
	E (GPa)	R (MPa)	E (GPa)	R (MPa)	E (GPa)	R (MPa)
$RMSE$	1.34	50.2	0.65	34.3	1.88	64.2
$CV_{RMSE}(\%)$	7.8	33.8	3.8	22.9	10.8	44.3

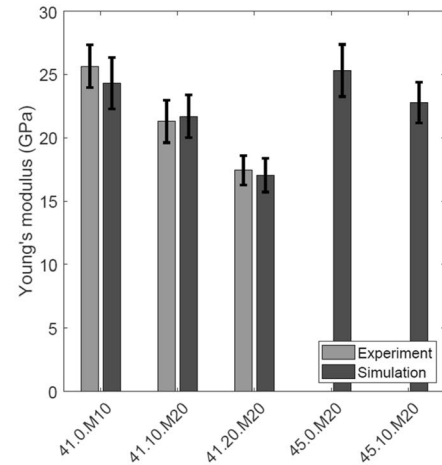
Table 4 Remaining input parameters for LHS based on their influence in the screening analysis (highlighted in gray), [28]

Input parameter	Relative influence of one standard deviation on Young's modulus for configuration:				
	41.0.M10	41.10.M20	41.20.M20	45.0.M20	45.10.M20
Φ_{GF}	2,2%	2,7%	3,7%	2,3%	2,8%
Φ_{Void}	-0,3%	-0,4%	-0,6%	-0,3%	-0,4%
E_{GF}	1,3%	1,6%	2,1%	1,5%	1,7%
$E_{UPPH,SMC}$	2,7%	3,4%	4,8%	2,6%	3,3%
Φ_{CF}	6,4%	5,6%	4,2%	6,1%	5,4%
$E_{1,CF}$	2,7%	2,2%	1,2%	2,6%	2,1%
Patch thickness	6,5%	5,2%	2,9%	6,2%	4,9%
Patch orientation	-0,2%	-2,5%	-3,0%	-0,1%	-2,3%

Fig. 4 Simulated and experimental uncertainties of Young's modulus for CoDiCo-SMC tensile specimen; error bars indicate one standard deviation [28]



(a) Realizations for configuration 41.0.M10



(b) Comparison of experiments and simulations

input parameters were sampled according to their probability distributions using LHS. Realizations of the uncertain Young's modulus including the fitted normal distribution are exemplarily shown in Fig. 4a for configuration 41.0.M10. The Young's modulus lies with approximately 95% confidence within the highlighted area. Simulated standard uncertainties are of similar size as the experimental standard deviations. Experimental and simulated standard uncertainties decrease with increasing CF misorientation for the same GF content (cf. Fig. 4b). The systematic deviation from the respective reference simulation with the smallest mesh possible (30,000 FE elements) was for all configurations below 5.3 MPa [28]. The overall uncertainty budget is given in Table 5, with the bias b given generally as the $RMSE$ of the configuration with 41 and 45 wt% FMF (cf. Table 3).

4.3 Surrogate modeling of FE simulation

Table 6 shows the $RMSE$ and the respective coefficient of variation of the surrogate models compared to test data, based on LHS generated FE simulations (P_1), the virtual

Table 5 Uncertainty budget for FE simulation of Young's modulus of CoDiCo-SMC tensile [28]

	41.0.M10	41.10.M20	41.20.M20	45.0.M20	45.10.M20
$u_{Sim,I}$	2016	1695	1326	2051	1601
$u_{Sim,D}$	5.3	0.3	1	3.2	0.1
$ b $			646		
$u_{c,Sim}$	2117	1813	1475	2151	1727
U_{Sim}	4234	3627	2951	4301	3453

experiments (FE simulations of different specimen configurations, P_2) and the real experiments (P_3). Additionally, the configurations no. 1 to 10 of the physical experiments were considered in P_{3*} .

When comparing P_1 and P_2 , the Kriging model predicted both the Young's modulus and the tensile strength slightly better than the ANN. In test set P_2 , only three distinct FMF in DiCo-SMC were contained. Hence, the covered parameter space was limited. Considering physical experiments (P_3), the bias substantially increased. However, the

Table 6 Systematic deviations (bias) of the surrogate models for CoDiCo-SMC tensile specimen [28]

	Kriging model		ANN	
	E (GPa)	R (MPa)	E (GPa)	R (MPa)
$RMSE(P_1)$	0.20	6.63	0.32	8.86
$CV_{RMSE}(P_1)$ (%)	1.2	4.8	1.9	6.5
$RMSE(P_2)$	0.10	26.00	0.42	30.04
$CV_{RMSE}(P_2)$ (%)	0.5	13.9	2.4	16.1
$RMSE(P_3)$	1.37	35.88	1.00	21.4
$CV_{RMSE}(P_3)$ (%)	8.0	24.1	5.8	27.2
$RMSE(P_{3*})$	0.65	24.99	0.47	23.10
$CV_{RMSE}(P_{3*})$ (%)	3.8	16.7	2.8	15.4

relative deviation is similar to the one of the FE simulation (cf. Table 3). Since the FE simulation could not correctly describe the behavior of the specimens with an excessively high fiber content, this is inevitably to be expected for the surrogate models trained on these FE simulations, too. Therefore, the comparison was made to P_{3*} , that consists of data from physical experiments of the specimens with 41 and 45 wt% FMF. Particularly the systematic deviation of the Young's modulus is significantly lower. The systematic deviation of the tensile strength is also lower in this test set but remains at a higher level. Nonetheless, the computational expense for the functional evaluation is drastically reduced by using surrogate models. A single FE simulation lasted 57 s on a system based with 3.3 GHz clock speed (Intel Core i5-6600). The same configuration was evaluated using the surrogate models in less than 0.01 s.

Using an overall sum of training data (810 in total), the iterative training approach is compared to a direct training, both for ANN and Kriging model (cf. Fig. 5). The final sum of training data was determined based on an assumed convergence of the Young's modulus. In each iteration, the ANN and the Kriging model were trained on the same training data. The ANN model performance was initially inferior compared to the reference ANN model trained on more data, both for Young's modulus and tensile strength. More training data was needed for the higher degrees of freedom in the ANN. This behavior was not observed for the Kriging model. Interestingly, the initial model performed already about 1% better than the reference in predicting Young's modulus. However, a repeated, second direct training led to comparable results for the direct Kriging model approach ($CV_{RMSE} = 2.1\%$ for Young's modulus and 4.7% for tensile strength). Here, the Kriging model improves only slightly using iterative training. A initial convergence is assumed. For this simple load case, no additional use by iterative training can be determined. However, investigations in Ref. [28] for a more complex load case in a flexural specimen showed advantages [28].

4.4 Measurement uncertainty of the surrogate models

Table 7 gives the overall uncertainty budget for the Young's modulus, using a coverage factor $k = 2$. Generally, the uncertainties of the models resulting from training and input variables hold for all test data sets. It is noteworthy that the uncertainty of the Kriging model based on training data is

Fig. 5 Evolution of surrogate model bias based on iterative (it) training data generation for tensile specimen for Young's modulus and tensile strength [28]

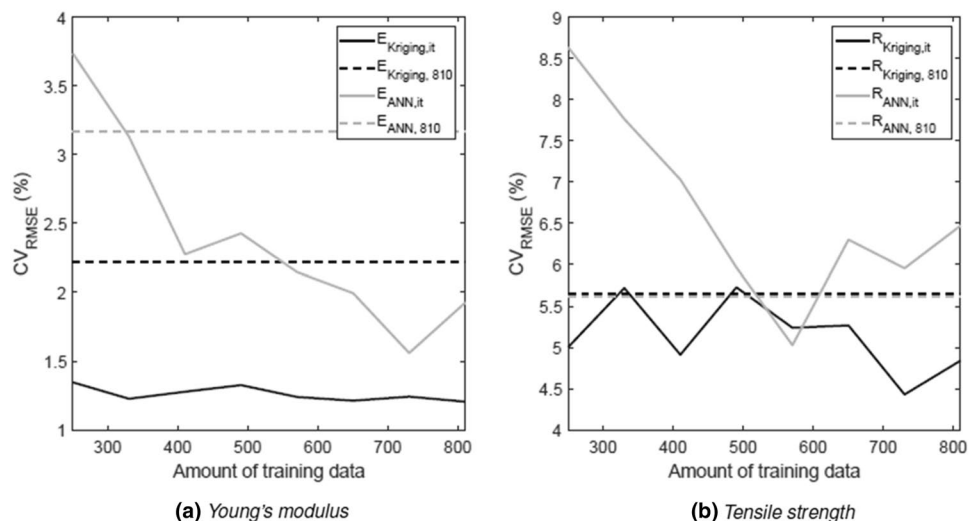


Table 7 Uncertainty budget for surrogate modeled Young's modulus of CoDiCo-SMC tensile specimen (MPa) [28]

	Kriging model				ANN			
	P_1	P_2	P_3	P_{3^*}	P_1	P_2	P_3	P_{3^*}
$u_{SM,I}$	684				1161			
$u_{SM,T}$	98				1908			
$ b $	200	95	1374	647	321	420	1001	473
$u_{c,SM}$	719	697	1538	947	2118	2334	2505	2344
U_{SM}	1439	1394	3079	1893	4637	4668	5009	4688

comparably low. Hence, a lower overall uncertainty results for the Kriging model due to the significantly lower contributions of the Kriging model terms $u_{SM,I}$ and $u_{SM,T}$ compared to the terms of the ANN. The model-related uncertainties contribute significantly to the overall uncertainty in both cases [28]

5 Conclusion and outlook

The local stress state highly influences the impact of delaminations on the tensile strength. CF misorientations lead to shear stresses in the tensile specimen. The combination of delamination and CF misorientations (specimen 41.20 and 41.20.M20 as well as 50.20 and 50.20.M20) significantly reduces the tensile strength in both experiments and simulations. This result of interacting defects stresses the importance of a function-oriented in-line defect assessment for the cost-efficient production of FRPs [28].

Parametrized FE simulations were conducted to analyze the influence of the manufacturing deviations. A measurement uncertainty analysis of the calculated Young's modulus showed that the fiber fraction and the thickness of the CF patch are of high relevance. Thus, they should be measured in addition to the patch orientation, the glass fiber fraction and potential delaminations to reduce the overall material uncertainty. Generally, the uncertainty of the FE simulations based on input parameters matched the experimental uncertainty. The expanded uncertainty of the FE simulation is approximately 20% of the expected specimen stiffness [28].

Two different surrogate models were trained based on parametrized FE simulations. The Kriging model performed better in predicting Young's modulus and tensile strength. It is to be highlighted that adequate simulations are required to build reliable surrogate models with low bias as simulations serve for surrogate model training. Being trained on simulations, surrogate model results follow the FE simulated experiments and not the experiments. The outliers of specimen 13 and 14 in Fig. 7 can be explained by the fact that the high analytical stiffness expectations of the simulations

(high FMF and Co-SMC) are located at the edge of the training data and are no longer correctly represented in the surrogate model. The surrogate model could probably not adjust appropriately. A remedy could be to further increase analytical FMF but this was not seen as relevant because of lacking technical relevance (poor fiber impregnation).

Generally, it is expected that the performance of the ANN would further improve with more training data. Surprisingly, the Kriging model reacted less sensitively to uncertain input variables than the FE models, leading to uncertainties lower than expected ($u_{Sim,I}$ compared to $u_{SM,I}$). Two influencing factors need to be considered in further investigations. First, uncertainties in material parameters were not further considered in the surrogate models to limit the training effort. Second, the training sets for the surrogate models were directly created from the global value domains, leading to comparatively large special distances between two respective training points. Consequently, the trained surrogate models may not correctly represent the influences of local variations due to uncertain input quantities in closer distances to a training point. The LHS generated global training data could be extended by material parameters and additionally adding local statistical fluctuations of the measured input quantities for training configuration. However, the training costs would be increased significantly [28].

In further steps, the strength prediction of the surrogate models needs to be revised. The FE simulations themselves, serving as training data, should be improved. Material parameters for the Co-SMC should be reviewed and more advanced damage models for the DiCo-SMC [36] could be used. Real measurements of the manufacturing deviations, based on thermography, industrial imaging, and Terahertz spectroscopy, can be integrated to demonstrate the in-line measurement approach [28]. A more complex load case shall be investigated.

Appendix

See Appendix Tables 8 and 9; Figs. 6 and 7.

Table 8 Material parameters used for FE simulation [28]

Parameter	Symbol	Value	Unit
Glass fiber diameter	d_{GF}	13.5	μm
Glass fiber length	l_{GF}	25.4	mm
Glass fiber Young's modulus	E_{GF}	73	GPa
Glass fiber Poisson's ratio	ν_{GF}	0.22	–
Nominal glass fiber content	Φ_{GF}	41	wt%
UPPH resin Young's modulus	E_{UPPH}	3.06	GPa
UPPH resin Poisson's ratio	ν_{UPPH}	0.3	–
Maximum principal stress GF-UPPH (41 wt%)	$R_{GF-UPPH,41}$	130	MPa
Maximum principal stress GF-UPPH (45 wt%)	$R_{GF-UPPH,45}$	154	MPa
Maximum principal stress GF-UPPH (50 wt%)	$R_{GF-UPPH,50}$	165	MPa
CF-UPPH Young's modulus 0°	$E_{ }$	110.1	GPa
CF-UPPH Young's modulus 90°	E_{\perp}	8.3	GPa
CF-UPPH shear modulus ($\perp $)	$G_{\perp }$	3.77	GPa
CF-UPPH shear modulus ($\perp\perp$)	$G_{\perp\perp}$	2.19	GPa
CF-UPPH Poisson's ratio ($\perp $)	$\nu_{\perp }$	0.27	–
CF-UPPH shear modulus ($\perp\perp$)	$\nu_{\perp\perp}$	0.33	GPa
CF-UPPH fiber content	Φ_{CF}	48	vol%
CF-UPPH longitudinal tensile strength	$R_{ }^{(+)}$	1424	MPa
CF-UPPH longitudinal compression strength	$R_{ }^{(-)}$	567	MPa
CF-UPPH transverse tensile strength	$R_{\perp}^{(+)}$	34	MPa
CF-UPPH transverse compression strength	$R_{\perp}^{(-)}$	163	MPa
CF-UPPH shear strength	$R_{\perp }$	79	MPa
Puck inclination parameter ($\perp +$)	$P_{\perp (+)}$	0.35	–
Puck inclination parameter ($\perp -$)	$P_{\perp (-)}$	0.3	–
Puck inclination parameter ($\perp\perp+$)	$P_{\perp\perp(+)}$	0.3	–
Puck inclination parameter ($\perp\perp-$)	$P_{\perp\perp(-)}$	0.3	–
Parameter for Puck weakening factor	M	0.5	–
Parameter for Puck weakening factor	S	0.5	–

Table 9 Input parameters and standard uncertainties, in-line measurable parameters in bold [28]

Input parameter	Distribution	Nominal value	Standard uncertainty
<i>Stiffness of DiCo-SMC</i>			
GF volume content (wt%)	Normal	41	2.25
Porosity (vol%)	Uniform	2	1.16
E_{GF} (GPa)	Uniform	73	3.8
ν_{GF}	Uniform	0.22	0.01
E_{UPPH} (GPa)	Uniform	3.06	0.68
ν_{UPPH}	Uniform	0.3	0.01
<i>Stiffness of Co-SMC</i>			
CF volume content (vol%)	Normal	48	2.5
$E_{CF, }$ (GPa)	Uniform	230	10.1
$E_{CF,\perp}$ (GPa)	Uniform	28	2.9
$G_{CF,\perp }$ (GPa)	Uniform	50	2.9
ν_{CF}	Uniform	0.23	0.01
<i>Delamination properties</i>			
Delamination length (mm)	Uniform	20	2.89
x-coordinate of delamination center (mm)	Uniform	0	2.89
<i>Co-SMC patch properties</i>			
Patch thickness (mm)	Normal	0.31	0.04
Patch orientation ($^\circ$)	Uniform	0	1.16

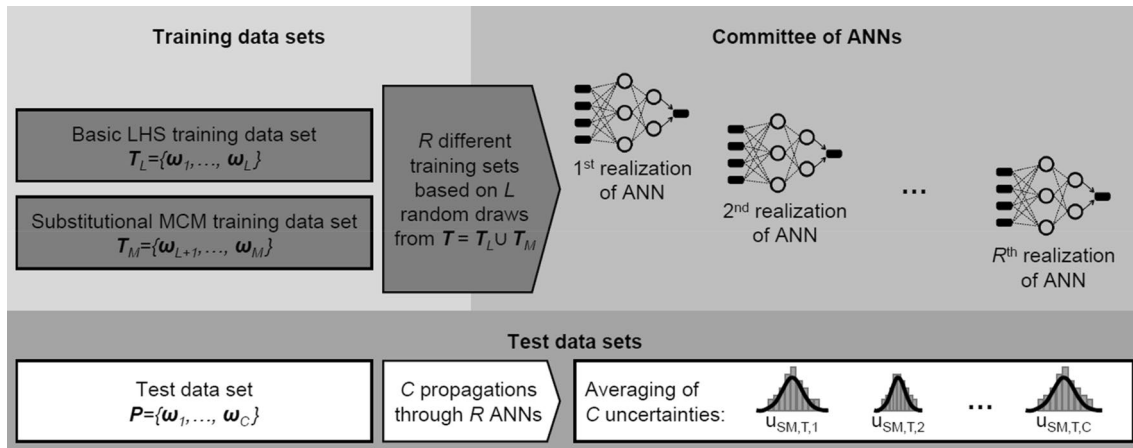
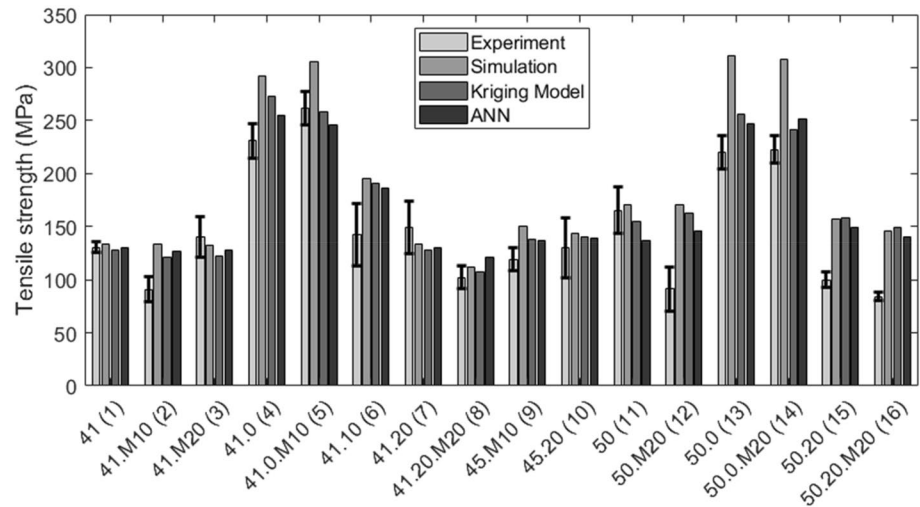


Fig. 6 Determination of the standard uncertainty due to model training data for an artificial neural network [27, 28]

Fig. 7 Experimental and simulated tensile strength for CoDiCo-SMC tensile specimen; error bars indicate one standard deviation; configuration no. in parenthesis; according to Ref. [28]



Acknowledgements The research documented in this paper has been funded by the German Research Foundation (DFG) within the International Research Training Group – Integrated engineering of continuous-discontinuous long fiber reinforced polymer structures – (GRK 2078). The support of the group by the German Research Foundation (DFG) is gratefully acknowledged.

Author contribution LB developed the main idea of the function-oriented quality assurance in hybrid SMC and initiated the bachelor thesis of DK and KD. The FE model was developed by LB, DK and KD. DK's work focused on the software development of the surrogate model. KD focused on the software implementation of the uncertainty analysis. KH supported the discussion of the results and thoroughly revised the paper. GL initiated the research subject, supervised the method development, supported the discussion of the results, thoroughly revised the paper, and served as Principal Investigator (PI).

Funding Open Access funding enabled and organized by Projekt DEAL.

Data availability The datasets generated during and/or analysed during the current study are not publicly available due to its size but are available from the corresponding author on reasonable request.

Declarations

Conflict of interest The authors declare no conflict of interest.

Open Access This article is licensed under a Creative Commons Attribution 4.0 International License, which permits use, sharing, adaptation, distribution and reproduction in any medium or format, as long as you give appropriate credit to the original author(s) and the source, provide a link to the Creative Commons licence, and indicate if changes were made. The images or other third party material in this article are included in the article's Creative Commons licence, unless indicated otherwise in a credit line to the material. If material is not included in the article's Creative Commons licence and your intended use is not permitted by statutory regulation or exceeds the permitted use, you will need to obtain permission directly from the copyright holder. To view a copy of this licence, visit <http://creativecommons.org/licenses/by/4.0/>.

References

1. European Commission (2019) Communication from the Commission to the European Parliament, the European Council, the Council, the European Economic and Social Committee and the Committee of the Regions—The European Green Deal. <https://eurlex.europa.eu/legal-content/EN/TXT/?uri=CELEX%3A52019DC0640>. Accessed 25 Aug 2022
2. Bücheler D (2018) Locally continuous-fiber reinforced sheet molding compound. Dissertation, Karlsruhe Institute of Technology (KIT). Fraunhofer, Stuttgart. <https://doi.org/10.5445/IR/1000079163>
3. Böhlke T, Henning F, Hrymak A, Kärger L, Weidenmann KA, Wood JT (2019) Continuous—discontinuous fiber-reinforced polymers—an integrated engineering approach, 1st edn. Carl Hanser, Munich. <https://doi.org/10.3139/9781569906934>
4. Fengler B, Schäferling M, Schäfer B, Bretz L, Lanza G, Häfner B, Hrymak A, Kärger L (2019) Manufacturing uncertainties and resulting robustness of optimized patch positions on continuous-discontinuous fiber reinforced polymer structures. *Compos Struct* 213:47–57. <https://doi.org/10.1016/j.compstruct.2019.01.063>
5. Talreja R (2015) Manufacturing defects in composites and their effects on performance. In: Irving P, Soutis C (eds) *Polymer composites in the aerospace industry*. Woodhead Publishing, Cambridge, pp 99–113. <https://doi.org/10.1016/B978-0-85709-523-7.00005-0>
6. Schäferling M, Häfner B, Lanza G, Trauth A, Weidenmann KA, Thompson M (2019) Effects of defects in hybrid sheet moulding compound—evaluation of defects and the impact on mechanical properties. *Mater Sci Eng Technol* 50(11):1317–1325. <https://doi.org/10.1002/mawe.201800139>
7. Bretz L, Häfner B, Lanza G (2021) Non-destructive measurement of fiber mass content of glass fiber sheet molding compound using Terahertz radiation. *Measurement* 168:108386. <https://doi.org/10.1016/j.measurement.2020.108386>
8. Schürmann H (2007) *Konstruieren mit Faser-Kunststoff-Verbunden*, 2nd edn. Springer, Berlin. <https://doi.org/10.1007/978-3-540-72190-1>
9. Franz M, Schleich B, Wartzack S (2019b) Variation analysis of design parameters of fibre-reinforced plastic parts. In: *Proceedings of the design society: international conference on engineering design*, Delft, 5–10 Aug 2019. Cambridge University Press, pp 2725–2734. <https://doi.org/10.1017/dsi.2019.279>
10. Franz M, Schleich B, Wartzack S (2021) Tolerance management during the design of composite structures considering variations

- in design parameters. *The International Journal of Advanced Manufacturing Technology* 113:1753–1770. <https://doi.org/10.1007/s00170-020-06555-5>
11. Kehrer L, Pinter P, Böhlke T (2017) Mean and full field homogenization of artificial long fiber reinforced thermoset polymers. In: *Proceedings of the 88th annual meeting in applied mathematics and mechanics*, Weimar, 6–10 Mar 2017. Wiley, pp 603–604. <https://doi.org/10.1002/pamm.201710271>
 12. Weckenmann A, Hartmann W (2013) Function-oriented method for the definition and verification of microstructured surfaces. *Precis Eng* 37(3):684–693. <https://doi.org/10.1016/j.precisioneng.2013.01.013>
 13. Weckenmann A, Hartmann W (2015) A model- and simulation-based approach for tolerancing and verifying the functional capability of micro/nano-structured workpieces. *Measurement* 76:70–79. <https://doi.org/10.1016/j.measurement.2015.08.010>
 14. Wagner R (2020) Strategien zur funktionsorientierten Qualitätsregelung in der Serienproduktion. Dissertation, Karlsruhe Institute of Technology (KIT). Shaker, Düren. <https://doi.org/10.5445/IR/1000124008>
 15. Gauder D, Wagner R, Gözl J, Häfner B, Lanza G (2019) Funktionorientierte Qualitätssicherung von Mikrozahnradern hinsichtlich des Geräuschverhaltens. *Tech Mess* 86(9):469–477. <https://doi.org/10.1515/teme-2019-0090>
 16. Sinsbeck M (2017) Uncertainty quantification for expensive simulations—optimal surrogate modeling under time constraints. Dissertation, University of Stuttgart. Opus, Stuttgart. <https://doi.org/10.18419/opus-9206>
 17. Häfner B, Biehler M, Wagner R, Lanza G (2018) Comparison of anomaly detection capabilities of pulse phase thermography in transmission and reflection setup on Sheet Molding Compound. In: *Online proceedings of the 15th CIRP conference on computer aided tolerancing*, Milan, 13–11 June 2018. Elsevier, pp 155–160. <https://doi.org/10.1016/j.procir.2018.04.031>
 18. Pfrommer J, Zimmerling C, Liu J, Kärger L, Henning F, Beyerer J (2018) Optimisation of manufacturing process parameters using deep neural networks as surrogate models. In: *Online proceedings of the 51st CIRP conference on manufacturing systems*, Stockholm, 16–18 May 2018. Elsevier, pp 426–431. <https://doi.org/10.1016/j.procir.2018.03.046>
 19. Greve L, van de Weg BP (2022) Surrogate modeling of parametrized finite element simulations with varying mesh topology using recurrent neural networks. *Array* 14:100137. <https://doi.org/10.1016/j.array.2022.100137>
 20. Hürkamp A, Lorenz R, Behrens B-A, Dröder K (2019) Computational manufacturing for multi-material lightweight parts. In: *Online proceedings of the 2nd CIRP conference on composite material parts manufacturing (CCMPM 2019)*, Sheffield, 10–11 Oct 2019. Elsevier, pp 102–107. <https://doi.org/10.1016/j.procir.2019.09.041>
 21. Lee J, Lee Y-J, Shim C-S (2020) Probabilistic prediction of mechanical characteristics of corroded strands. *Eng Struct* 203:109882. <https://doi.org/10.1016/j.engstruct.2019.109882>
 22. Dey S, Mukhopadhyay T, Adhikari S (2017) Metamodel based high-fidelity stochastic analysis of composite laminates: a concise review with critical comparative assessment. *Compos Struct* 171:227–250. <https://doi.org/10.1016/j.compstruct.2017.01.061>
 23. Wang C, Qiang X, Xu M, Wu T (2022) Recent advances in surrogate modeling methods for uncertainty quantification and propagation. *Symmetry* 14(6):1219. <https://doi.org/10.3390/sym14061219>
 24. JCGM100 (2008) Evaluation of measurement data—Guide to the expression of uncertainty in measurement (GUM). Joint Committee for Guides in Metrology. <https://www.bipm.org/en/committees/jc/jcgm/publications>. Accessed 25 Aug 2022
 25. JCGM101 (2008) Evaluation of measurement data—supplement 1 to the “Guide to the expression of uncertainty in measurement”—propagation of distributions using a Monte Carlo method. Joint Committee for Guides in Metrology. <https://www.bipm.org/en/committees/jc/jcgm/publications>. Accessed 25 Aug 2022
 26. Lord G, Wright L (2003) Uncertainty evaluation in continuous modelling. NPL Report. CMSC 31/03. Teddington: National Physical Laboratory. <https://eprintspublications.npl.co.uk/2900/>. Accessed 25 Aug 2022
 27. Coral R, Flesch CA, Penz CA, Roisenberg M, Pacheco A (2016) A monte carlo-based method for assessing the measurement uncertainty in the training and use of artificial neural networks. *Metrology and Measurement Systems* 23(2):281–294. <https://doi.org/10.1515/mms-2016-0015>
 28. Bretz L (2022) Function-oriented in-line quality assurance of hybrid sheet molding compound. Dissertation, Karlsruhe Institute of Technology (KIT). Shaker, Düren. <https://doi.org/10.5445/IR/1000147740>
 29. Zhang P (1993) Model selection via multifold cross validation. *The Annals of Statistics* 21.1, pp 299–313. <http://www.jstor.org/stable/3035592>. Accessed 25 Aug 2022
 30. Deutsches Institut für Normung e.V (2019) Plastics—determination of tensile properties—Part 1: general principles. DIN EN ISO 527-1:2019-12. Beuth, Berlin. <https://www.beuth.de/en/standard/din-en-iso-527-1/306958894>. Accessed 25 Aug 2022
 31. Gross D, Seelig T (2018) Fracture mechanics: with an introduction to micromechanics, 3rd edn. Springer, Berlin. <https://doi.org/10.1007/978-3-319-71090-7>
 32. Kremer T. KLuB-VDI2014 v2.0: Subroutine zur Festigkeitsanalyse von Faser-Kunststoff-Verbunden nach der VDI-Richtlinie 2014, Teil 3 für ABAQUS. https://www.klub.tu-darmstadt.de/media/fachgebiet_klub/downloads_3/KLuB-VDI2014_v2.zip. Accessed 25 Aug 2022
 33. Bouhlel MA, Hwang JT, Bartoli N, Lafage R, Morlier J, Martins JR (2019) A Python surrogate modeling framework with derivatives. *Adv Eng Softw* 135:102662. <https://doi.org/10.1016/j.advengsoft.2019.03.005>
 34. Verein Deutscher Ingenieure e.V. (2006) Development of FRP components—analysis. VDI 2014 Part 3:2006-09. Beuth, Berlin. <https://www.beuth.de/en/technicalrule/vdi-2014-blatt-3/71840061>. Accessed 25 Aug 2022
 35. Trauth A (2018) Characterisation and modelling of continuous-discontinuous sheet moulding compound composites for structural applications. Dissertation, Karlsruhe Institute of Technology (KIT). KIT Scientific Publishing, Karlsruhe. <https://doi.org/10.5445/KSP/1000097160>
 36. Görthofer J, Meyer N, Pallicy TD, Schöttl L, Trauth A, Schemmann M, Hohberg M, Pinter P, Elsner P, Henning F, Hrymak A, Seelig T, Weidenmann KA, Kärger L, Böhlke T (2019) Virtual process chain of sheet molding compound: Development, validation and perspectives. *Compos B Eng* 169:133–147. <https://doi.org/10.1016/j.compositesb.2019.04.001>

Publisher's Note Springer Nature remains neutral with regard to jurisdictional claims in published maps and institutional affiliations.